





Room temperature biaxial magnetic anisotropy in $\text{La}_{0.67}\text{Sr}_{0.33}\text{MnO}_3$ thin films on SrTiO_3 buffered MgO (001) substrates for spintronic applications

Cite as: Appl. Phys. Lett. **113**, 052403 (2018); <https://doi.org/10.1063/1.5020072>

Submitted: 19 December 2017 . Accepted: 19 July 2018 . Published Online: 03 August 2018

 Sandeep Kumar Chaluvadi, Fernando Ajejas,  Pasquale Orgiani, Olivier Rousseau,  Giovanni Vinai, Aleksandr Yu Petrov, Piero Torelli, Alain Pautrat, Julio Camarero, Paolo Perna, and  Laurence Mechin



View Online



Export Citation



CrossMark

ARTICLES YOU MAY BE INTERESTED IN

[The role of strain in magnetic anisotropy of manganite thin films](#)

Applied Physics Letters **71**, 140 (1997); <https://doi.org/10.1063/1.119454>

[Strain-dependent magnetic phase diagram of epitaxial \$\text{La}_{0.67}\text{Sr}_{0.33}\text{MnO}_3\$ thin films](#)

Applied Physics Letters **76**, 2421 (2000); <https://doi.org/10.1063/1.126363>

[Magnetic anisotropy, damping, and interfacial spin transport in Pt/LSMO bilayers](#)

AIP Advances **6**, 055212 (2016); <https://doi.org/10.1063/1.4950971>

HIDEN
ANALYTICAL

Instruments for **Advanced Science**

- Knowledge,
- Experience,
- Expertise

[Click to view our product catalogue](#)

Contact Hiden Analytical for further details:

www.HidenAnalytical.com
info@hiden.co.uk



Gas Analysis

- ▶ dynamic measurement of reaction gas streams
- ▶ catalysis and thermal analysis
- ▶ molecular beam studies
- ▶ dissolved species probes
- ▶ fermentation, environmental and ecological studies



Surface Science

- ▶ UHVTPD
- ▶ SIMS
- ▶ end point detection in ion beam etch
- ▶ elemental imaging - surface mapping



Plasma Diagnostics

- ▶ plasma source characterization
- ▶ etch and deposition process reaction kinetic studies
- ▶ analysis of neutral and radical species



Vacuum Analysis

- ▶ partial pressure measurement and control of process gases
- ▶ reactive sputter process control
- ▶ vacuum diagnostics
- ▶ vacuum coating process monitoring



Room temperature biaxial magnetic anisotropy in $\text{La}_{0.67}\text{Sr}_{0.33}\text{MnO}_3$ thin films on SrTiO_3 buffered MgO (001) substrates for spintronic applications

Sandeep Kumar Chaluvadi,¹ Fernando Ajejas,^{2,3} Pasquale Orgiani,^{4,5} Olivier Rousseau,¹ Giovanni Vinai,⁴ Aleksandr Yu Petrov,⁴ Piero Torelli,⁴ Alain Pautrat,⁶ Julio Camarero,^{2,3} Paolo Perna,² and Laurence Mechin^{1,a)}

¹Normandie Univ, UNICAEN, ENSICAEN, CNRS, GREYC, 14000 Caen, France

²IMDEA-Nanociencia, Campus de Cantoblanco, 28049 Madrid, Spain

³Universidad Autónoma de Madrid, Campus de Cantoblanco, 28049 Madrid, Spain

⁴CNR-IOM TASC National Laboratory, Area Science Park-Basovizza, 34149 Trieste, Italy

⁵CNR-SPIN, UOS Salerno, 84084 Fisciano, SA, Italy

⁶Normandie Univ, UNICAEN, ENSICAEN, CNRS, CRISMAT, 14050 Caen, France

(Received 19 December 2017; accepted 19 July 2018; published online 3 August 2018)

Spintronics exploits the magnetoresistance effects to store or sense the magnetic information. Since the magnetoresistance strictly depends on the magnetic anisotropy of a system, it is fundamental to set a defined anisotropy to the system. Here, we investigate half-metallic $\text{La}_{0.67}\text{Sr}_{0.33}\text{MnO}_3$ thin films by means of vectorial Magneto-Optical Kerr Magnetometry and found that they exhibit pure biaxial magnetic anisotropy at room temperature if grown onto a MgO (001) substrate with a thin SrTiO_3 buffer. In this way, we can avoid unwanted uniaxial magnetic anisotropy contributions that may be detrimental for specific applications. The detailed study of the angular evolution of the magnetization reversal pathways and critical fields (coercivity and switching) discloses the origin of the magnetic anisotropy, which is magnetocrystalline in nature and shows fourfold symmetry at any temperature. © 2018 Author(s). All article content, except where otherwise noted, is licensed under a Creative Commons Attribution (CC BY) license (<http://creativecommons.org/licenses/by/4.0/>). <https://doi.org/10.1063/1.5020072>

Half-metallic perovskite oxides promise great advantages over conventional spintronic metallic materials for applications such as magnetic sensors, magnetic random access memory (MRAM) devices, magnetic tunnel junctions (MTJs), and domain wall race-track memory devices.¹ Perovskite oxides, in general, appear to be new contenders for many novel applications that were considered traditionally beyond their range.² The conduction mechanism in these materials, in fact, strongly depends on the interplay between orbital and spin degrees of freedom³ that may be exploited to add multiferroic or ferroelectric functionalities.^{4–6} The complexity of such a mechanism, however, can determine entangled magnetotransport response which becomes undesired in some cases. For example, it has been observed that a switchable anisotropic magnetoresistance (AMR) response in manganites may be hidden by the colossal magnetoresistance (CMR) if the magnetic anisotropy of the system is not accurately designed.⁷ Irrespective of the applications, one of the key properties that need to be considered for a ferromagnetic sample is the magnetic anisotropy that dictates the magnetization reversal pathways as well as the MR output.⁸ While a defined *uniaxial anisotropy* is essential for magnetic field sensors based on AMR,⁷ a *biaxial anisotropy*, which provides four stable magnetization states, has the capability to encode more information (four binary bits: “00,” “01,” “10,” “11”) and can be used in memory and logic devices.^{9,10} However, especially in half-metallic perovskite compounds with fourfold magnetocrystalline anisotropy in bulk, it

remains difficult to avoid either strain (induced by the substrate) or shape uniaxial anisotropy in thin films.^{11,12}

Among manganites, $\text{La}_{0.67}\text{Sr}_{0.33}\text{MnO}_3$ (LSMO) has arisen special interest for its peculiar properties such as nearly 100% spin polarization and room temperature (RT) ferromagnetism with a Curie temperature of about $T_c \sim 370$ K, hence enabling RT spintronic applications. The magnetotransport properties of these compounds in thin films are strongly affected by external perturbations such as substrate-induced strain.¹³ In general, in tensile (compressive) strained films, the electron occupancy in the “ e_g ” doublet favors in-plane (out-of-plane) x^2-y^2 ($3z^2-r^2$) orbitals¹⁴ determining the in-plane (out-of-plane) magnetization easy axis.¹⁵ In addition, tensile (compressive) strain reduces (enhances) T_c with respect to the bulk value.^{16,17} Therefore, the choice of the substrate for the LSMO growth is extremely important. The most commonly used single crystal substrate is SrTiO_3 (STO) ($a_{\text{STO}} = 0.3905$ nm) with (001) crystallographic orientation since LSMO ($a_{\text{LSMO}} = 0.387$ nm) grown epitaxially on STO exhibits low tensile strain (0.82%) and has good structural and morphological properties.¹⁸ However, in the low thickness regime, a sizeable uniaxial (twofold) anisotropy contribution¹⁹ due to surface steps and terraces originated from the mis-cut angle of the substrate^{7,11,20,21} generally hides the biaxial (fourfold) magnetocrystalline anisotropy of the LSMO film. In the higher thickness regime, LSMO on STO (001) usually shows a competition between (biaxial) bulk¹² and shape or strain (uniaxial) magnetic anisotropy.²² Another single crystal oxide that can be used as a substrate for the growth of LSMO films is MgO with (001) crystallographic orientation. However, the lattice mismatch between LSMO

^{a)} Author to whom correspondence should be addressed: laurence.mechin@ensicaen.fr



and MgO ($a_{\text{MgO}}=0.4212$) results in large tensile strain ($\sim 8\%$). This generally degrades the film magneto-transport and morphological properties that limited their use.

One of the utmost challenges is to control the magnetic anisotropy of the system via substrate-induced strain and surface engineering. In this letter, to define magnetic anisotropy symmetry in LSMO thin films, instead of growing it directly on cubic STO (001) crystals, we deposited a 50 nm LSMO film on the cubic MgO (001) substrate and employed 12 nm STO as a buffer layer. The inclusion of a 12 nm STO buffer layer on the MgO substrate not only helps in incorporating the structural and interfacial defects in it but also minimizes the misfit strain and acts as a template for depositing a good quality epitaxial LSMO film. The angular dependent magnetic anisotropy symmetry in our STO buffered LSMO films shows dominant biaxial anisotropy even at RT, enhanced by an order of magnitude at 40 K.

The STO (001) buffered LSMO thin films were epitaxially grown on the MgO (001) substrate by pulsed laser deposition (PLD) from commercial stoichiometric targets by using the KrF excimer laser of wavelength 248 nm. High energetic laser pulses ($1.4\text{--}1.7\text{ J/cm}^2$) were used for transferring the correct elemental ratio of heavy elements for growing stoichiometric LSMO and STO films.^{23,24} The deposition was performed at an oxygen pressure of 0.35 mbar while maintaining the substrate temperature at 720°C . After deposition, the samples were cooled down to RT at 10°C per minute at an oxygen pressure of 7×10^2 mbar. The thicknesses of LSMO and STO layers were set at 50 and 12 nm, respectively. The structural, morphology, magnetic, and electrical transport measurements were performed using PANalytical X'Pert four-circle X-Ray Diffraction (XRD) in low and high-resolution modes, Atomic Force Microscopy (AFM), a Superconducting Quantum Interference Device (SQUID), and the four-probe technique, respectively. Angular dependent *in-plane* magnetization reversal process, coercivity, and magnetic anisotropy measurements were performed at 300 K and 40 K by using vectorial Magneto-Optical Kerr ($v\text{-MOKE}$) magnetometry.²⁵

The overall optimal structural and compositional properties of the film are confirmed by the transport and morphological properties. In fact, resistivity and magnetization vs. temperature measurements (see Fig. S1 in the [supplementary material](#)) demonstrate low residual resistivity, Metal-Insulator transition temperature " T_{MI} ," and Curie temperature " T_{C} " close to the bulk values, i.e., >420 and 362 K, respectively, whereas T_{MI} of the LSMO film, when directly grown on MgO (001), showed a reduced value ($T_{\text{MI}} \sim 325$ K) (see Fig. S2 [supplementary material](#)). Therefore, the STO buffer layer helps to reduce structural defects in the LSMO layer and improves the film properties. The film surface probed by AFM reveals an RMS (root mean square) roughness of about 0.35 nm (very smooth, i.e., less than one unit cell). The epitaxial structure of the STO and LSMO films is demonstrated by the $\theta\text{-}2\theta$ XRD spectrum that shows only (001) peaks, indicating the preferential *c*-axis orientation along the [001] substrate crystallographic direction [Fig. 1(a)]. The calculated "*c*" lattice parameters of STO and LSMO films are 0.3903 and 0.3873 nm, respectively, which indirectly indicate the optimal oxygen composition in the

film.²⁶ In order to determine the in-plane epitaxial relationship between the LSMO film and the MgO (001) substrate, azimuthal ϕ -scans are performed around the (0-24) MgO and (0-13) LSMO asymmetric reflections, as shown in Fig. 1(b). The peaks with a separation of 90° observed for both the MgO substrate and the LSMO film demonstrate the four-fold symmetry with the [100] plane of the film parallel to the [100] plane of the substrate.

In order to investigate in detail the LSMO film structure, we have recorded the XRD reciprocal space map (RSM) around the asymmetric (0-13) LSMO and (0-24) MgO reflections. Interestingly, in the low-resolution mode [Fig. 2(a)], a single diffraction peak is evident, thus inferring the cubic structure of the film (i.e., identical in-plane lattice parameters, $a=b$). However, in the high-resolution mode [i.e., using a Ge (220) double-bounce monochromator], the RSM around the (0-13) LSMO crystallographic reflection shows a double-peak structure along the Q_x in-plane direction [inset of Fig. 2(a)]. Such a feature indicates the presence of two slightly different in-plane lattice parameters (i.e., $a \neq b$), thus supporting a possible orthorhombic or monoclinic structure for the LSMO film. The average in-plane lattice parameter of LSMO is 0.388 nm, which is very close to the relaxed pseudocubic lattice value. Figure 2(b) shows the omega scans measured around the LSMO (002) peak at different ϕ angles (0° , 45° , and 90°). At $\phi = 0^\circ$ and 90° , the

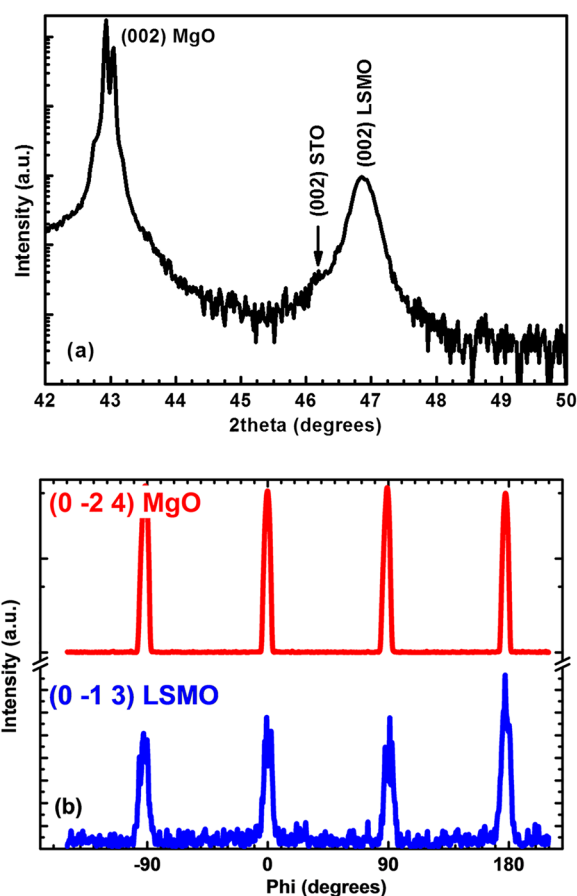


FIG. 1. (a) Theta-2 theta XRD scan of the 50 nm thick LSMO film on the STO buffered MgO (001) substrate and (b) asymmetrical Phi scans around the (0-13) peak of the LSMO (001) film and the (0-24) peak of the MgO (001) substrate show 90° separation cube-on-cube epitaxy.

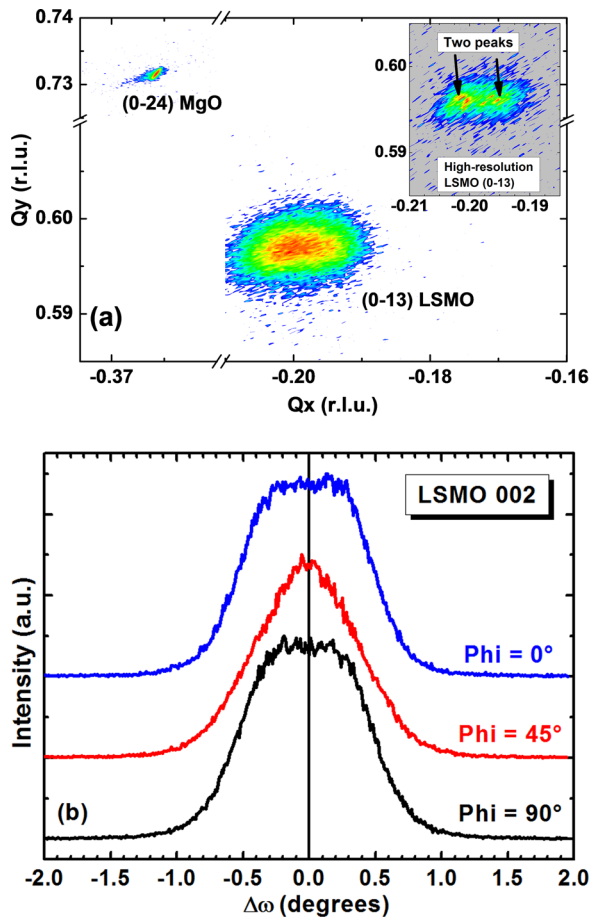


FIG. 2. (a) Low-resolution RSM scans of (0-13) LSMO and (0-24) MgO peaks show that the LSMO film is fully relaxed. The inset presents the high-resolution RSM scan of (0-13) LSMO that shows two peaks, marked with arrows. (b) Omega scans measured around the LSMO (002) peak at different phi angles, i.e., 0° , 45° , and 90° .

presence of the double peak along the LSMO out-of-plane direction indicates, as a first approximation, the presence of two LSMO domains with the *c*-axis direction tilted at $\sim 0.4^\circ$ with respect to the [001]-MgO direction. However, the rocking curve taken at $\phi = 45^\circ$ does not show any double-peak structure, which excludes a possible rhombohedral arrangement of the LSMO unit cells. Therefore, from the phi scans ($\alpha = \beta = 90^\circ$) and omega scans ($\gamma \neq 90^\circ$), we deduce that the most probable scenario is that the LSMO structure is monoclinic with in-plane fourfold symmetry and out-of-plane rigid rotations of the LSMO cell.

The magnetic anisotropy of the film also reveals a four-fold symmetry. This was investigated at RT in detail by acquiring *in-plane* Kerr hysteresis loops by *v*-MOKE in the full angular range (i.e., 0° – 360°) while keeping fixed the external magnetic field direction. At $\theta = 0^\circ$, the applied external magnetic field is aligned parallel to the [100] crystallographic axis of the MgO (001) substrate. By exploiting the simultaneous acquisition of two in-plane magnetization components, i.e., parallel [$M_{\parallel}(H)$] and perpendicular [$M_{\perp}(H)$], we can deduce the symmetry of magnetic anisotropy present in the film.^{7,11,27} In fact, by inspecting the change of sign in $M_{\perp}(H)$, we can accurately locate the easy axis (e.a.) and hard axis (h.a.) directions. Figure 3 presents the normalized Kerr hysteresis loops of the LSMO (001) film

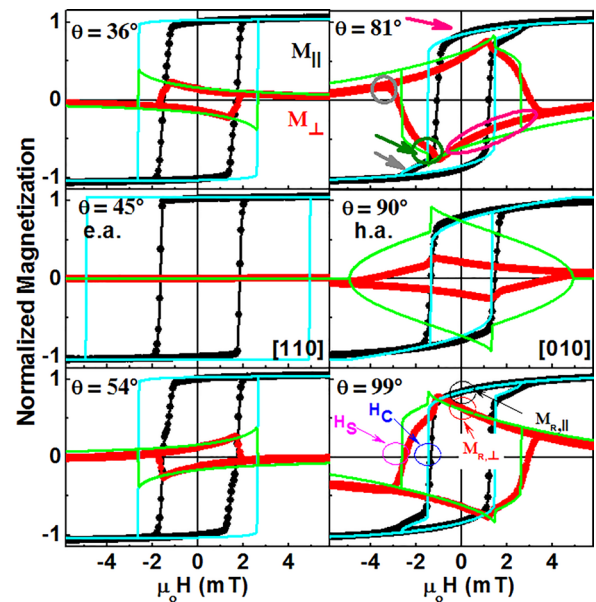


FIG. 3. Normalized magnetic hysteresis cycles of the 50 nm thick LSMO film grown on STO buffered MgO (001) measured by *v*-MOKE at 300 K at and around the easy (e.a.) (left) and hard (h.a.) (right) axes. The corresponding applied external magnetic field angles (θ) with respect to the crystallographic axis are specified. The $M_{\parallel}(H)$ (black) and $M_{\perp}(H)$ (red) loops acquired simultaneously are shown. The arrow (circles) in the top right panel indicates the double transition, which is the signature of biaxial anisotropy. The cyan and green solid lines correspond to the simulation results of the Stoner-Wohlfarth model.

acquired at and around e.a. and h.a., i.e., $\theta = 45^\circ$, 90° , and $\pm 9^\circ$. The square loop with sharp irreversible transitions in $M_{\parallel}(H)$ is found at $\theta = 45^\circ$, whereas the $M_{\perp}(H)$ component is almost zero. This indicates that the magnetization is aligned in the film plane either parallel or anti-parallel, which corresponds to a magnetization reversal proceeding by nucleation and further propagation of magnetic domains (characteristic of an e.a. behavior). When the field is applied away from the e.a., smoother reversible transitions are found, indicating that the reversal starts by rotation followed by propagation of domains. In particular, when the magnetic field is applied around the e.a., i.e., from $\theta = 36^\circ$ to 54° , the magnetization switches with just one irreversible transition and from the $M_{\perp}(H)$ component, we could observe that there is a significant change of sign. This means that the magnetization rotates within the film plane in clockwise to anticlockwise directions or vice-versa with respect to the applied field angle. The remanence of $M_{\parallel}(H)$ at the e.a. is $M_{R,\parallel} \cong M_S$, and the coercive field is about 1.8 mT.

The $M(H)$ loops taken at $\theta = 81^\circ$ and $\theta = 99^\circ$ show that the magnetization reversal takes place in three steps, which are marked with arrows in $M_{\parallel}(H)$ and circles in $M_{\perp}(H)$ [Fig. 3 (top right)], respectively. Sweeping the field from positive to negative values, the reversal occurs by a first reversible magnetization rotation, followed by two irreversible transitions that take place by nucleation and propagation of two consecutive 90° domain walls.²⁸ At h.a., i.e., $\theta = 90^\circ$, as the field strength decreases, the $M_{\parallel}(H)$ loop shows rotation of the magnetization followed by sharp irreversible transition and final rotation towards the applied field direction. The reversal proceeds thus with one (two) irreversible transition, related to nucleation and propagation of 180° (90°) domain

walls, when the field is applied close to one of the two e.a. (h.a.) orientations of magnetization. These are the typical signatures of a fourfold magnetic symmetry.²⁷ The experimental data have been properly reproduced in the whole angular range with a modified coherent rotation Stoner-Wohlfarth model^{11,27} by using exclusively a single magnetic anisotropy term with fourfold symmetry whose strength was extracted from the experimental curves in the hard axis ($H_K^b = 5$ mT). Note that, since this model is based on coherent rotation, it fails to reproduce the experimental data in the regions in which nucleation and propagation of domain mechanisms dominate (i.e., close to e.a.). However, it provides a qualitative and quantitative estimation of the relevant anisotropy contributions involved (in the h.a. region).

The fourfold symmetry of the magnetic anisotropy becomes more evident by plotting the angular dependent remanence and critical fields in the full angular range (Fig. 4). The normalized remanence magnetization plots ($M_{R,\parallel}/M_S$ and $M_{R,\perp}/M_S$) extracted from the experimental $M_{\parallel}(H)$ and $M_{\perp}(H)$ loops at the applied field $\mu_0 H = 0$ as a function of angle “ θ ” are shown in Fig. 4(a). Both the magnetization components show repeated features with the periodicity of 90° . In addition, $M_{R,\perp}$ changes its sign for every 45° , i.e., whenever it crosses the characteristic axes. The polar plots of $M_{R,\parallel}/M_S$ and $M_{R,\perp}/M_S$ are presented in panels (c) and (d) of Fig. 4, revealing the fourfold symmetry. In particular, $M_{R,\parallel}/M_S$ resembles a butterfly structure with the highest and lowest values pointing towards e.a. and h.a. of the film, i.e., along with the [110] and [010] crystallographic directions, whereas $M_{R,\perp}/M_S$ shows a four lobe symmetrical shape with positive and negative values which are depicted in solid and open circles.

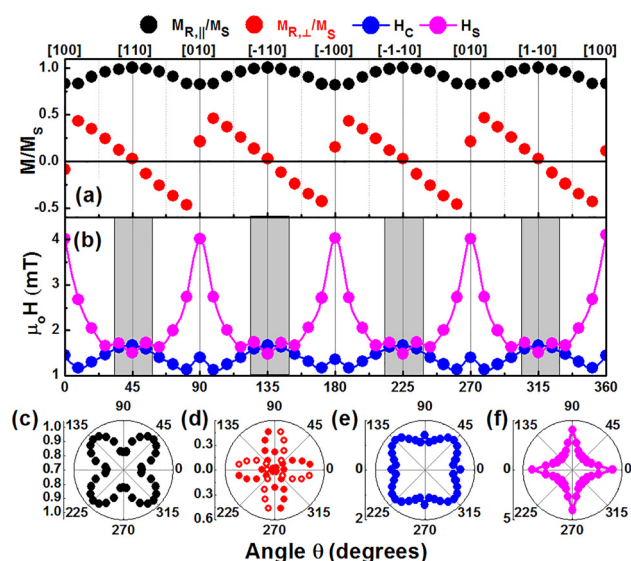


FIG. 4. Angular evolution at 300 K of the magnetic properties of the 50 nm thick LSMO film grown on the STO buffered MgO (001) substrate. (a) Normalized remanence magnetization $M_{R,\parallel}/M_S$ (black) and $M_{R,\perp}/M_S$ (red) and (b) critical fields [coercivity “ H_C ” (blue) and switching “ H_S ” (magenta)] as a function of the applied field angle “ θ ” show well-defined 90° periodicity, i.e., a pure bi-axial anisotropy. The grey shaded regions in (b) indicate that the system exhibits only one irreversible transition, whereas the white regions indicate that the system exhibits two consecutive irreversible transitions. (c)–(f) Polar plots of $M_{R,\parallel}/M_S$, $M_{R,\perp}/M_S$, H_C , and H_S , respectively. Positive and negative values in (d) are represented by solid and open circles.

Figure 4(b) shows the angular dependence of the critical fields, i.e., coercive (H_C) and switching (H_S) fields, extracted from $M_{\parallel}(H)$ and $M_{\perp}(H)$ loops. The value of “ H_C ” (H_S) is higher (lower) at e.a., i.e., [110], and decreases (increases) as it approaches towards h.a., i.e., [010]. H_C and H_S coincide at and around e.a. which correspond to one irreversible transition (grey shaded area), leading to 180° domain wall reversals. As the field is applied away from the e.a. (i.e., approaching the h.a., white region), H_S increases and reaches the maximum exactly at the h.a. In the white shaded regions, the magnetization reversal takes place with two irreversible transitions that are related to the nucleation and propagation of two consecutive 90° domain walls. The polar plots of H_C and H_S are presented in Figs. 4(e) and 4(f) which show symmetrical four lobes and an asteroid shape, respectively, with 90° periodicity. From these angular dependent analyses, it is evident that the angles between two adjacent e.a. and h.a. are orthogonal to each other and the minima of $M_{R,\parallel}$ at the consecutive h.a. have identical values, which experimentally prove that no uniaxial magnetic anisotropy contribution exists.²⁷ These features demonstrate the fourfold symmetry of the magnetic anisotropy in the LSMO/STO/MgO (001) structure, which is similar to the magnetocrystalline anisotropy of the bulk LSMO with easy axes aligned towards 45° [110].²⁹ The analysis of both magnetization components therefore discloses the symmetry of the magnetic anisotropy with high accuracy. Note that, even though the authors in Ref. 12 claim to have biaxial anisotropy in the LSMO/STO film, the difference between the magnetization remanence states at two consecutive h.a. reveals an additional uniaxial contribution, as explained by the authors in Refs. 19 and 27.

In order to disclose the nature of the fourfold magnetic anisotropy in our systems, we performed temperature dependent studies. The normalized Kerr hysteresis loops [Fig. 5(a)] measured at 40 K in different in-plane magnetic field directions present similar features and symmetry with respect to the RT case. The e.a. and h.a. are present at 45° [110] and 90° [010]. Near h.a., i.e., at $\theta = 70^\circ$ and 80° , two irreversible transitions are observed owing to nucleation and propagation of two consecutive 90° domain walls. In this case, the data have been reproduced by again using a single magnetic anisotropy term with fourfold anisotropy and the anisotropy field is one order of magnitude larger than the one found at RT ($H_K^b = 40$ mT). Temperature-dependent coercive fields [Fig. 5(b)] in the angular range of 0° – 180° have 90° periodicity as the RT behavior but with a tremendous increase in the coercive fields of about one order of magnitude. Therefore, as the temperature decreases from 300 K to 40 K, the signatures of biaxial anisotropy become more evident. The cause of anisotropy is due to magnetocrystalline anisotropy of LSMO, which is usually dominant at low temperatures.³⁰

In summary, we have fabricated high-quality epitaxial LSMO thin films on the STO buffered MgO (001) substrate by the PLD technique and studied *in-plane* magnetic anisotropy properties at 300 and 40 K. We demonstrated that the use of the STO buffer layer improved the quality of the LSMO film by accommodating structural defects. The LSMO film has a 4-domain monoclinic structure with domains present along [100] and [010] directions. The magnetic anisotropy also

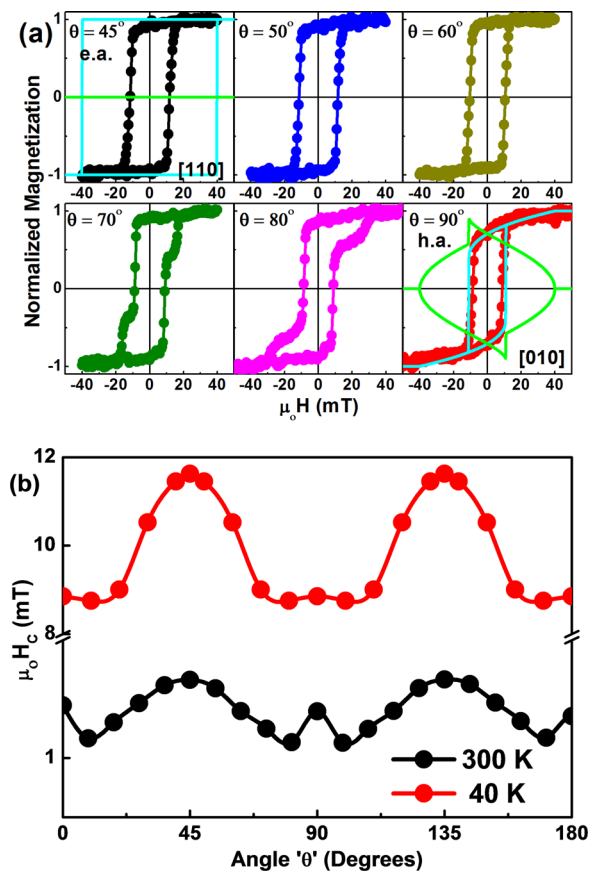


FIG. 5. (a) Normalized magnetic hysteresis loops of the 50 nm thick LSMO film grown on STO buffered MgO (001) around the first half quadrant measured at 40 K and (b) angular dependent coercive field “ H_c ” at 40 and 300 K. The cyan and green solid lines in (a) correspond to the simulation results of the Stoner-Wohlfarth model.

showed biaxial anisotropy with the e.a. direction which is aligned towards 45° or [110], where the tilted domains are absent and the h.a. is aligned along the tilted monoclinic domains, i.e., 0° or [100]. As temperature decreases, the strength of the biaxial anisotropy increases, which is one order of magnitude larger at 40 K, revealing its magnetocrystalline origin. Unlike the LSMO films directly grown on STO (001) substrates that show anomalies in magnetic anisotropy, films that were grown onto STO buffered MgO (001) substrates display well-defined biaxial anisotropy, which can be useful in four bit logic devices based on purely anisotropic magnetoresistance response.

See [supplementary material](#) for the morphology, magnetic, and electrical transport properties of the LSMO/STO/MgO (001) film.

S.K.C. acknowledges Programme International de Coopération Scientifique (PICS) du CNRS under Grant No. 6161 and SIMEM Doctoral School at Université de Caen Normandie for financial support. IMDEA-Nanociencia acknowledges support from the “Severo Ochoa” Program for Centres of Excellence in R&D (MINECO, Grant No. SEV-2016-0686). F.A., J.C., and P.P. acknowledge the support of Spanish MINECO Project Nos. FIS2015-67287-P and

FIS2016-78591-C3-1-R and the Comunidad de Madrid through Project NANOFRONTMAG CM. This project has received funding from the European Union’s Horizon 2020 research and innovation programme under Grant Agreement Nos. 737116 (byAxon) and 654360 NFFA-Europe.

- ¹S. S. P. Parkin, M. Hayashi, and L. Thomas, *Science* **320**, 190 (2008).
- ²J. Heber, *Nature* **459**, 28 (2009).
- ³E. Dagotto, *Science* **309**, 257 (2005).
- ⁴F. A. Cuellar, Y. H. Liu, J. Salafranca, N. Nemes, E. Iborra, G. Sanchez-Santolino, M. Varela, M. G. Hernandez, J. W. Freeland, M. Zhernenkov, M. R. Fitzsimmons, S. Okamoto, S. J. Pennycook, M. Bibes, A. Barthélémy, S. G. E. Te Velthuis, Z. Sefrioui, C. Leon, and J. Santamaria, *Nat. Commun.* **5**, 4215 (2014).
- ⁵M. Bibes, *Nat. Mater.* **11**, 354 (2012).
- ⁶N. A. Spaldin and R. Ramesh, *MRS Bull.* **33**, 1047 (2008).
- ⁷P. Perna, D. Maccariello, F. Ajejas, R. Guerrero, L. Méchin, S. Flament, J. Santamaria, R. Miranda, and J. Camarero, *Adv. Funct. Mater.* **27**, 1700664 (2017).
- ⁸P. Perna, C. Rodrigo, M. Muñoz, J. L. Prieto, A. Bollero, D. Maccariello, J. L. F. Cuñado, M. Romera, J. Akerman, E. Jiménez, N. Mikuszeit, V. Cros, J. Camarero, and R. Miranda, *Phys. Rev. B* **86**, 24421 (2012); P. Perna *et al.*, *Appl. Phys. Lett.* **104**, 202407 (2014); P. Perna *et al.*, *Phys. Rev. B* **92**, 220422 (2015).
- ⁹M. V. Pitke, *Czech. J. Phys. B* **21**, 467 (1971).
- ¹⁰M. Salehi-Fashami and N. D’Souza, *J. Magn. Magn. Mater.* **438**, 76 (2017).
- ¹¹P. Perna, C. Rodrigo, E. Jiménez, F. J. Teran, N. Mikuszeit, L. Méchin, J. Camarero, and R. Miranda, *J. Appl. Phys.* **110**, 13919 (2011); **109**, 07B107 (2011).
- ¹²Y. Suzuki, H. Y. Hwang, S.-W. Cheong, and R. B. van Dover, *Appl. Phys. Lett.* **71**, 140 (1997).
- ¹³C. Adamo, X. Ke, H. Q. Wang, H. L. Xin, T. Heeg, M. E. Hawley, W. Zander, J. Schubert, P. Schiffer, D. A. Muller, L. Maritato, and D. G. Schlom, *Appl. Phys. Lett.* **95**, 112504 (2009).
- ¹⁴D. Pesquera, G. Herranz, A. Barla, E. Pellegrin, F. Bondino, E. Magnano, F. Sánchez, and J. Fontcuberta, *Nat. Commun.* **3**, 1189 (2012).
- ¹⁵J. Dho, Y. N. Kim, Y. S. Hwang, J. C. Kim, and N. H. Hur, *Appl. Phys. Lett.* **82**, 1434 (2003).
- ¹⁶A. J. Millis, T. Darling, and A. Migliori, *J. Appl. Phys.* **83**, 1588 (1998).
- ¹⁷P. Perna, L. Méchin, M. P. Chauvat, P. Ruterana, C. Simon, and U. Scotti di Uccio, *J. Phys. Condens. Matter* **21**, 306005 (2009).
- ¹⁸Y. Feng, K. J. Jin, L. Gu, X. He, C. Ge, Q. H. Zhang, M. He, Q. L. Guo, Q. Wan, M. He, H. Bin Lu, and G. Yang, *Sci. Rep.* **6**, 22382 (2016).
- ¹⁹S. K. Chaluvadi, P. Perna, F. Ajejas, J. Camarero, A. Pautrat, and S. Flament, and L. Méchin, *J. Phys. Conf. Ser.* **903**, 12021 (2017).
- ²⁰H. K. Lee, I. Barsukov, A. G. Swartz, B. Kim, L. Yang, H. Y. Hwang, and I. N. Krivorotov, *AIP Adv.* **6**, 55212 (2016).
- ²¹M. Mathews, F. M. Postma, J. C. Lodder, R. Jansen, G. Rijnders, and D. H. A. Blank, *Appl. Phys. Lett.* **87**, 242507 (2005).
- ²²R. M. Reeve, C. Mix, M. König, M. Foerster, G. Jakob, and M. Kläui, *Appl. Phys. Lett.* **102**, 122407 (2013).
- ²³G. Z. Liu, Q. Y. Lei, and X. X. Xi, *Appl. Phys. Lett.* **100**, 202902 (2012).
- ²⁴P. Orgiani, R. Ciancio, A. Galdi, S. Amoruso, and L. Maritato, *Appl. Phys. Lett.* **96**, 032501 (2010).
- ²⁵E. Jiménez, N. Mikuszeit, J. L. F. Cuñado, P. Perna, J. Pedrosa, D. Maccariello, C. Rodrigo, M. A. Niño, A. Bollero, J. Camarero, and R. Miranda, *Rev. Sci. Instrum.* **85**, 53904 (2014); J. L. F. Cuñado, J. Pedrosa, F. Ajejas, A. Bollero, P. Perna, F. J. Teran, R. Miranda, and J. Camarero, *Rev. Sci. Instrum.* **86**, 046109 (2015).
- ²⁶P. Orgiani, A. Y. Petrov, R. Ciancio, A. Galdi, L. Maritato, and B. A. Davidson, *Appl. Phys. Lett.* **100**, 042404 (2012).
- ²⁷D. Ecija, E. Jiménez, N. Mikuszeit, N. Sacristán, J. Camarero, J. M. Gallego, J. Vogel, and R. Miranda, *Phys. Rev. B* **77**, 24426 (2008); J. L. F. Cuñado, J. Pedrosa, F. Ajejas, P. Perna, R. Miranda, and J. Camarero, *J. Phys.: Condens. Matter* **29**, 405805 (2017).
- ²⁸J. L. Costa-Krämer, D. M. Borsari, J. M. García-Martín, M. S. Martín-González, D. O. Boerma, and F. Briones, *Phys. Rev. B* **69**, 144402 (2004).
- ²⁹M. Konoto, T. Kohashi, K. Koike, T. Arima, Y. Kaneko, Y. Tomioka, and Y. Tokura, *Appl. Phys. Lett.* **84**, 2361 (2004).
- ³⁰K. Steenbeck and R. Hiergeist, *Appl. Phys. Lett.* **75**, 1778 (1999).